

Backbone Heterojunction Photocatalysts for Efficient Sacrificial Hydrogen Production

Richard J. Lyons, Rhys J. Bourhill, Ewan McQueen, Sam D. Harding, Krzysztof Pawlak, Thomas Fellowes, Harry W. Capps, Alexander J. Cowan, Andrew I. Cooper, Adrian M. Gardner,* Martijn A. Zwijnenburg,* and Reiner Sebastian Sprick*

A common strategy to improve the efficiency of organic photocatalysts for hydrogen production from aqueous mixtures is to create bulk heterojunction nanoparticles comprised of intermixed donor and acceptor phases that allow for efficient charge separation after photoexcitation. However, many of these systems possess poor stability due to aggregation of these nanoparticles under operating conditions. Moreover, the use of surfactants, that inhibit aggregation and promote donor–acceptor phase intermixing, can form an insulating barrier that reduces the photocatalytic efficiency of these nanoparticles. Here, these issues are bypassed by preparing a single-component organic heterojunction-type polymer, P40, in which a molecular donor, pyrene, is tethered to poly(fluorene-*co*-dibenzo[*b,d*]thiophene sulfone), a conjugated polymer acceptor. By tethering the donor and acceptor together, phase intermixing is guaranteed without the need for costly post-synthesis processing or insulating surfactants. Moreover, the influence of pyrene in P40 is determined to be multifaceted, as it influences the dynamics of the excited state, the aggregate microstructure, and the local solvent environment. P40 is found to have an exceptional external quantum efficiency of 38% at 420 nm in the presence of triethylamine as a hole scavenger, the highest value reported for any linear conjugated polymer to date for sacrificial hydrogen production.

1. Introduction

We currently face a climate crisis due to the excessive consumption of fossil fuels;^[1] yet, this consumption will persist until viable alternative fuels are developed. Solar energy is the most abundant energy source available to us, however, the diurnal cycle limits the availability of solar energy to the daytime.^[2] But by capturing and converting solar energy into a chemical fuel, we can make solar energy available at the point of demand. One such chemical fuel is elemental hydrogen. Hydrogen can be burned in air to perform useful work^[3] or can be used in fuel cells to generate electricity directly^[4] with the only by-product of each process being water. Hydrogen is also a necessary chemical feedstock for the refinement of hydrocarbons and the production of essential fertilizers by way of the Haber-Bosch process.^[5–7] The direct splitting of water into hydrogen and oxygen using solar energy and a photocatalyst is, potentially,


R. J. Lyons, S. D. Harding, K. Pawlak, T. Fellowes, A. I. Cooper
Materials Innovation Factory and Department of Chemistry
University of Liverpool
Liverpool L7 3NY, UK

R. J. Bourhill, E. McQueen, R. S. Sprick
Department of Pure and Applied Chemistry
University of Strathclyde
Glasgow G1 1XL, UK
E-mail: sebastian.sprick@strath.ac.uk

H. W. Capps, A. J. Cowan, A. M. Gardner
Department of Chemistry and Stephenson Institute of Renewable Energy
University of Liverpool
Liverpool L69 7ZD, UK

E-mail: adrian.gardner@liverpool.ac.uk
H. W. Capps, A. J. Cowan, A. M. Gardner
Early Career Laser Laboratory
University of Liverpool
Liverpool L69 3BX, UK

M. A. Zwijnenburg
Department of Chemistry
University College London
London WC1H 0AJ, UK
E-mail: m.zwijnenburg@ucl.ac.uk

 The ORCID identification number(s) for the author(s) of this article can be found under <https://doi.org/10.1002/adfm.202513025>

© 2025 The Author(s). Advanced Functional Materials published by Wiley-VCH GmbH. This is an open access article under the terms of the [Creative Commons Attribution](#) License, which permits use, distribution and reproduction in any medium, provided the original work is properly cited.

DOI: 10.1002/adfm.202513025

the most convenient approach to generating elemental hydrogen due to the relative simplicity of photocatalytic systems.^[8]

Over a half-century worth of research has been dedicated to the development of water splitting photocatalysts,^[9] much of which has focused on the development and implementation of inorganic semiconductors as photocatalysts.^[10] While large strides have been made, most inorganic photocatalysts reported that are capable of driving overall water splitting can only operate in the UV region of the solar spectrum;^[11] a region that accounts for only $\approx 5\%$ of the energy available from sunlight.^[12] This low sensitivity to much of the solar spectrum by inorganic photocatalysts severely limits their applicability for real-world application as their solar-to-hydrogen conversion efficiencies (STH) fall below the necessary 10%.^[11] Organic semiconductors, on-the-other-hand, often possess relatively narrower optical gaps, absorbing light further into the visible region of the solar spectrum than their inorganic counterparts.^[13] Moreover, organic materials provide excellent versatility due to the comparative ease in which their physical and optoelectronic properties can be altered by chemical modification.^[13] This has resulted in significant efforts being devoted toward the development of conjugated organic materials for photocatalytic hydrogen evolution in recent years, with various chemical structures and architectures being explored, including covalent organic frameworks (COFs),^[14] conjugated microporous polymers (CMPs),^[15,16] small molecules/oligomers,^[17–20] and linear polymers.^[21–26]

To develop more efficient photocatalysts, organic materials are often processed into multi-component bulk heterojunctions (BHJs) by exploiting the solubility of many organic semiconductor materials. Typically, these are composed of molecular acceptors and soluble donor polymers,^[20,27,28] although alternative configurations have been reported.^[29–31] Provided sufficient care has been taken during the design stage, BHJ-type photocatalysts are often more efficient than their constituents in isolation or as physical mixtures.^[27,28,32] This increased efficiency is, typically, attributed to efficient charge transfer and separation between the donor and acceptor components; a process that separates the tightly bound Frenkel excitons generated after photoexcitation and inhibits charge recombination.^[33] For these systems, efficient mixing of the individual components is facilitated by solution phase processing into nanoparticles; primarily via mini-emulsion processing or nanoprecipitation.^[34] Nanoparticle preparation often, but not always, necessitates the use of surfactants to inhibit aggregation, improve hydrophilicity,^[34,35] or promote efficient mixing of the donor/acceptor phases.^[27] Yet, issues remain with these BHJ-type photocatalysts, such as surfactants inhibiting charge transfer^[36,37] and the stability of nanoparticles under long-term operation having been regularly highlighted in recent years.^[29,38] Particularly, control over the morphology is required, as the issue of poor miscibility between the donor and acceptor components sometimes has resulted in phase separation in to pure donor and pure acceptor domains, rather than as an intermixed donor–acceptor phase.^[30] A noteworthy example of this was reported by Kosco et al., who observed donor–acceptor phase separation into a core–shell morphology that resulted in a significant drop in photocatalytic performance that they ascribed to the confinement of photoelectrons to the accep-

tor core.^[27] Additionally, good interfacing between components in photocatalytic systems has been shown to be of great importance in recent years, particularly in biohybrid systems.^[39,40] Recently, this approach has been extended to ternary systems^[41] and controlled templated COF heterojunctions,^[42] yet careful design and control at either the synthesis or processing stages was necessary to provide adequate control over phase intermixing for these examples.

Alternatively, directly tethering the donor and acceptor components together using covalent bonds would provide excellent interfacing and allow for efficient charge transfer while concurrently suppressing phase separation.^[43,44] Moreover, this would circumvent the time consuming solution phase processing that is often used to prepare BHJ-type photocatalysts. Various architectures of these so-called single-component materials have been reported for application in organic photovoltaic devices, these architectures include block co-polymers, molecular dyads/triads, and double-cable polymers (outlined in **Figure 1**).^[43] Unlike the well-studied push-pull-type polymers, direct conjugation between the donor and acceptor components is inhibited.^[43] Despite promising results for these materials in photovoltaics, few examples have been translated to photocatalytic systems for hydrogen evolution with only dyads^[45] and block copolymers^[46] having been explored.

Here, we present **P40** (**Figure 2a**), a double-cable-type single-component photocatalyst in which the molecular donor pyrene (**Py**) is tethered to the conjugated polymer acceptor, poly(fluorene-co-dibenzo[*b,d*]thiophene sulfone) (**FS**). This non-conventional configuration of molecular donor and polymer acceptor is similar in concept to our recently reported work on BHJ-type photocatalysts.^[29] **P40** was predicted to possess a type-II energy level offset between **FS** (acceptor) and **Py** (donor) with nanoscale separation between the components that was expected to promote efficient charge separation after photoexcitation. Importantly, as **Py** was bonded at the bridgehead of fluorene, direct conjugation, and therefore through bond charge transfer, between the **FS** backbone and **Py** was inhibited. **P40** was benchmarked against **P35**, the dimethyl functionalized **FS**-type polymer (**Figure 2a**),^[47,48] to better understand how the inclusion of **Py** influenced **P40**. The photocatalytic performance of **P40** for sacrificial hydrogen evolution was studied in a 1:1:1 mixture of water, triethylamine (TEA) and methanol (MeOH), where **P40** was found to have exceptionally high photocatalytic efficiency for sacrificial hydrogen evolution with an external quantum efficiency of 38% at 420 nm. This EQE represents one of the highest values reported to date for an organic photocatalyst for sacrificial hydrogen evolution. Using a combination of transient absorption spectroscopy (TAS) and computational predictions, the photophysical behavior of **P40** was studied in detail to better understand why **P40** shows such high efficiency for sacrificial hydrogen evolution. Nitrogen sorption isotherms showed that **P40** has an apparent Brunauer–Emmett–Teller surface area (S_{BET}) over three times greater than that of **P35**, which suggests that the inclusion of **Py** also changes the microstructure of **P40**. Therefore, the influence of **Py** in **P40** must extend beyond purely being a molecular donor and it must also play a significant role in determining the polymer's microstructure and also influences how **P40** interacted with the local solvent environment.

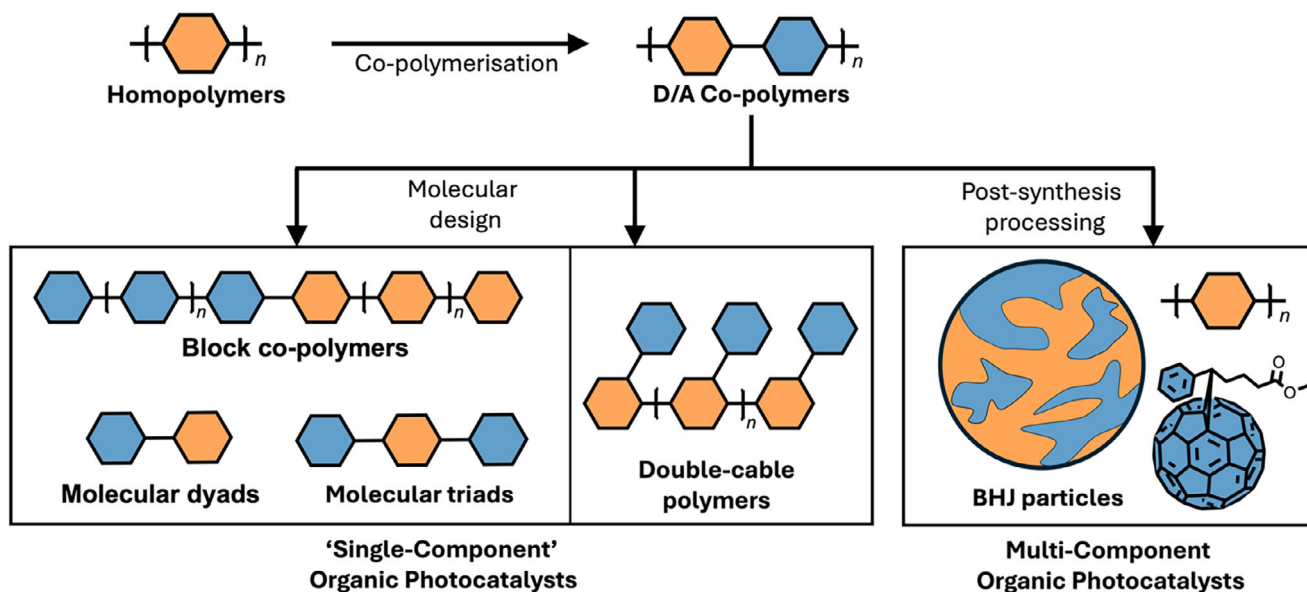


Figure 1. Schematic representation of the typical routes of developing organic semiconductor photocatalysts with greater efficiencies, including homopolymers, donor–acceptor (D/A) co-polymers, BHJ systems, molecular dyads and triads, block co-polymers, and double-cable polymers.

2. Results

2.1. Synthesis and Characterization

P35 and **P40** (Figure 2a) were synthesized via a typical Suzuki polycondensation reaction in *N,N*-dimethylformamide (DMF) at 150 °C using $[\text{Pd}(\text{PPh}_3)_4]$ as the catalyst. Full details of the synthesis and characterization are outlined in the Supporting Information. The characterization details of **P35** have been outlined in detail elsewhere.^[25,47,48] Thermogravimetric analysis (TGA) of **P40** showed that it possessed good thermal stability under air ($T_d = 399$ °C, 5 wt.% loss). Transmission Fourier transform infrared spectroscopy (FT-IR) analysis of **P40** showed the expected peaks of the aromatic C–H stretches at ≈ 3000 cm^{-1} and the characteristic asymmetric stretching vibrations of the sulfone group at 1300 and 1155 cm^{-1} . No long-range order was observed in the powder X-ray diffraction (PXRD) pattern of **P40**, suggesting that the as prepared polymer is amorphous. The apparent Brunauer–Emmett–Teller surface areas (S_{BET}) of **P35** and **P40** were determined by obtaining nitrogen sorption isotherms at 77 K. Both **P40** and **P35** are porous with specific surface areas of 346 and 109 $\text{m}^2 \text{g}^{-1}$, respectively. Residual Pd from the polymer synthesis – a known impurity that can act as a co-catalyst for proton reduction^[49–51] – was determined to be 0.19 wt.% for **P40** by inductively coupled plasma optical emission spectroscopy (ICP-OES). This is somewhat lower than the quantity determined for **P35** used here (0.58 wt.%). The particle sizes of **P35** and **P40** were determined using static light scattering (SLS) in a 1:1:1 water/TEA/MeOH mixture. Particle sizes were determined based on the Sauter mean diameter of the particles and were determined to be 2.90, and 1.19 μm for **P35**, and **P40**, respectively.

The optical gaps of **P35**, **P40**, and **Py** were estimated from the absorption onset of the powders in the solid-state (Figure 2c). **P35** and **P40** were found to have comparable optical gaps of 2.57 (483 nm) and 2.63 (471 nm) eV, respectively. Whereas **Py** was de-

termined to have a larger optical gap of 2.71 eV (458 nm). Unlike **P35**, that possesses a broad, featureless absorption profile, spanning from its onset to 300 nm, **P40** has a clear absorption maximum at ≈ 420 nm. The emission maxima of **P35**, **P40**, and **Py** were determined from the steady-state photoluminescence (PL) spectra of the powders in the solid-state (Figure 2d). For **P35** and **P40**, the emission maxima are located at ≈ 480 nm, whereas **Py** has a slightly blue shifted emission maximum (472 nm).

2.2. Photocatalysis Experiments

Organic photocatalysts are typically unable to perform overall water splitting as their shallow ionization potentials (IPs) lack the thermodynamic overpotential to drive the water oxidation half reaction, a fact that necessitates the use of sacrificial electron donors (SEDs). Here, we utilized TEA as a SED in a 1:1:1 mixture of water/TEA/MeOH, as this mixture has been used in previous studies involving **P35** for photocatalytic hydrogen evolution.^[25,47] The intended role of MeOH was to aid in dispersing **P40**, however it was also found that MeOH acted as both a SED and a proton source in the presence of **P40**, though its activity was markedly lower than when aqueous TEA was used (Figure S40, Supporting Information). Hydrogen evolution experiments were performed using a 300 W Xe light source equipped with a 420 nm long pass filter (>420 nm). The photocatalytic performance of powders of **Py**, **P35**, and **P40** (Figure 3a) were studied and a physical mixture of **Py** and **P35** (**P35-Py**) was also tested.

At low concentrations (5 mg in 22.5 mL of 1:1:1 water/TEA/MeOH), there is a stark difference in photocatalytic performance between **P35** and **P40** (Figure 3a). At these concentrations, **P35** has a photocatalytic rate of 2.22 $\text{mmol h}^{-1} \text{g}^{-1}$ (1.11 $\mu\text{mol h}^{-1}$), whereas **P40** has a much higher photocatalytic rate of 24.0 $\text{mmol h}^{-1} \text{g}^{-1}$ (120 $\mu\text{mol h}^{-1}$), an almost tenfold difference. However, upon increasing the photocatalyst

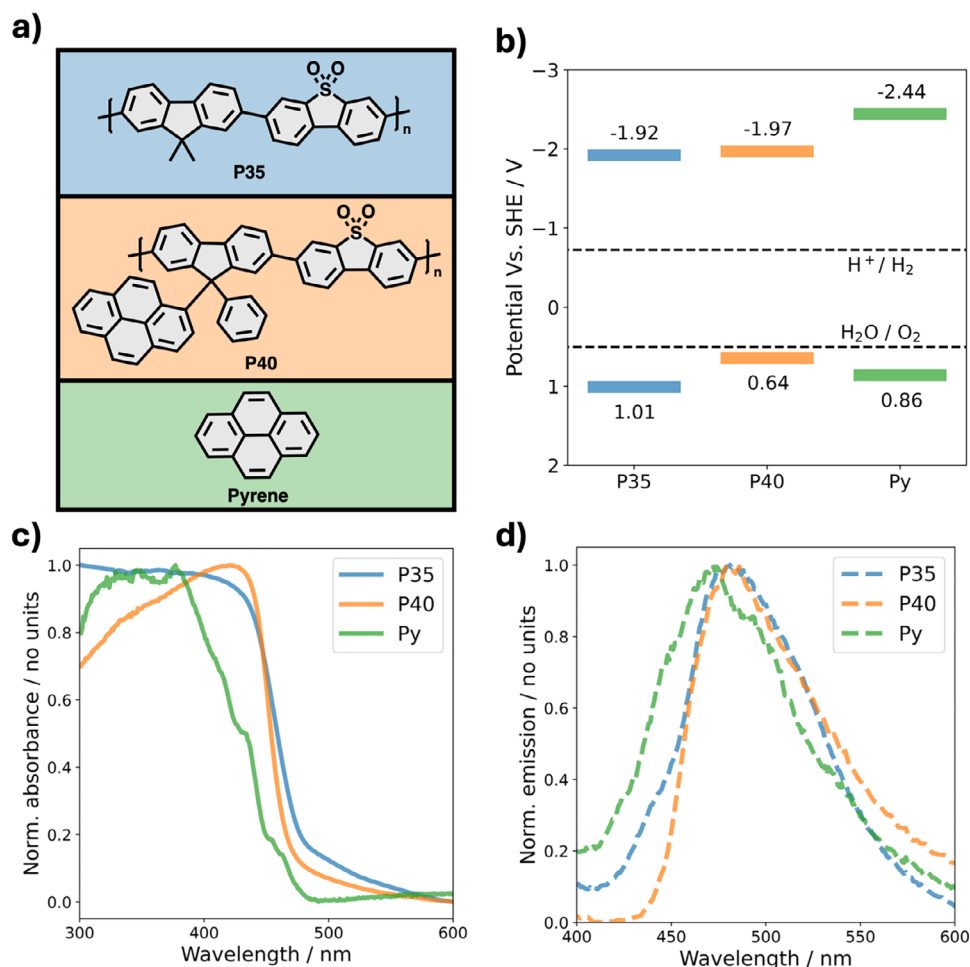


Figure 2. a) The chemical structures of **Py**, **P35**, and **P40**. b) The DFT predicted ionization potentials (IPs) and electron affinities (EAs) of the polymers and the proton reduction and water oxidation potentials. The proton reduction and water oxidation potentials shown in panel b are for a pH of 12.3, the pH of a 1:1:1 mixture of water/TEA/MeOH. The normalized steady-state c) UV-vis absorption spectra and d) PL spectra ($\lambda_{\text{exc}} = 360 \text{ nm}$) of **Py**, **P35**, and **P40** powders.

concentration fourfold (25 mg in 22.5 mL of 1:1:1 water/TEA/MeOH, Figure 3b), the difference in rate becomes less pronounced, with the mass normalized hydrogen evolution rate of **P40** decreasing to $12.2 \text{ mmol h}^{-1} \text{ g}^{-1}$ ($305.9 \text{ } \mu\text{mol h}^{-1}$) and the rate of **P35** increasing to $6.0 \text{ mmol h}^{-1} \text{ g}^{-1}$ ($149.0 \text{ } \mu\text{mol h}^{-1}$). We should highlight, however, that the absolute rate of **P40** did indeed increase with increasing photocatalyst concentration and the decrease in mass normalized rate is due to the deflating effect of mass normalization on photocatalyst rates at higher photocatalyst concentrations. These results strongly suggest that **P40** is an efficient hydrogen evolution photocatalyst at very low photocatalyst concentrations when compared with **P35**.

The hydrogen evolution rate of the physical mixture of **P35** and **Py**, **P35-Py**, is $5.0 \text{ mmol h}^{-1} \text{ g}^{-1}$ ($125.9 \text{ } \mu\text{mol h}^{-1}$), slightly less than that of pure **P35**. Negligible hydrogen was observed for **Py** over a 5 h period, which is unsurprising given that, unlike **P35** and **P40** that possess residual Pd from the synthesis, **Py** was not loaded with noble metal co-catalysts, which are typically necessary for organic materials to generate hydrogen.^[52]

We estimated the EQEs of **P35** and **P40** to be 2.4% and 38.0%, respectively, in a 1:1:1 mixture of water/TEA/MeOH at 420 nm at a photocatalyst concentration of 1.0 mg mL^{-1} (full details outlined in Supporting Information). The EQE of **P40** exceeds **P35** by almost a factor of 16, a somewhat surprising observation given the rate of **P40** is only ≈ 2 times greater than **P35** at a similar concentration (see Figure 3c,d). When the concentration of **P35** was increased to 2.0 mg mL^{-1} the EQE was also found to increase to 6.4%; confirming that the concentration of **P35** is a limiting factor in these experiments. We believe that the difference between the photocatalytic rates (≈ 2 times greater) and the EQE (≈ 6 times greater) for **P40** compared with **P35** is due to the shorter path length used in the EQE measurements that permits more photons to be transmitted compared to the kinetic measurements, despite the greater concentration used for the EQE measurements. Our confidence in the superior EQE value determined for **P40** is reinforced by our transient absorption analysis (vide infra) that suggests stark differences in the excited state dynamics of **P35** and **P40**, specifically **P40** demonstrated a significantly larger polaron yield after photoexcitation than **P35**.

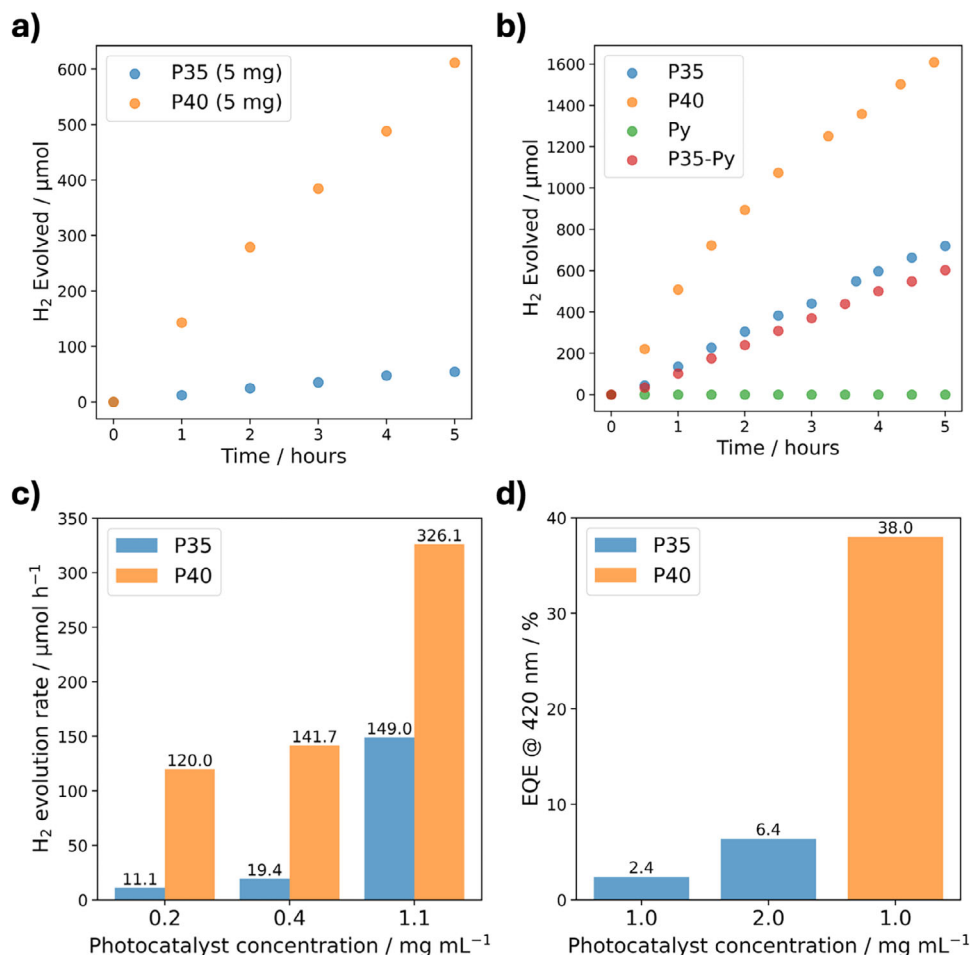


Figure 3. a) Hydrogen evolved versus time for 5 mg of **P35** and **P40** in 22.5 mL of 1:1:1 water/TEA/MeOH. b) The hydrogen evolution rates of 25 mg of **Py**, **P35**, **P40**, and **P35-Py** in 22.5 mL of 1:1:1 water/TEA/MeOH. c) Bar chart of the rates of **P35** and **P40** at mass loadings of 5, 10, and 25 mg in 22.5 mL of 1:1:1 water/TEA/MeOH. d) The external quantum efficiencies for **P35** and **P40** at 420 nm in 1:1:1 water/TEA/MeOH, the EQE of **P35** was recorded at concentrations of 1.0 and 2.0 mg mL⁻¹ due to the sensitivity of **P35** to concentration, whereas **P40** was recorded at a concentration of 1.0 mg mL⁻¹. Full details outlined in Sections S1.5.2. and S1.5.3. (Supporting Information).

Crucially, **P40** demonstrates one of the highest EQE values for any single-component organic photocatalyst for sacrificial hydrogen evolution and, to the best of our knowledge, represents the highest EQE reported for a linear polymer photocatalyst to date for sacrificial hydrogen evolution without the need for additional noble metal co-catalysts, solely relying on the residual palladium (0.19 wt.%) from the synthesis. The next highest reported EQE appears to be by Han et al., in which they reported an EQE of 30.48% at 520 nm in 0.1 ascorbic acid with 1 wt.% Pt (see Table S12, Supporting Information).^[53] While higher EQE values exceeding 80% have been reported,^[20,54] these materials have required nanoscale processing to achieve these efficiencies.

Longer-term stability of **P40** in a 1:1:1 mixture of water/TEA/MeOH was studied over more than 45 h under visible light irradiation (Figure S35, Supporting Information). The material was found to be active for the entire duration of the experiment and post-catalysis FT-IR and PL spectra showed no significant differences compared to the material as made (Figure S36, Supporting Information). However, static light scattering experiments show that there was some degree of aggregation of **P40** fol-

lowing the extended run (Figure S37, Supporting Information); potentially explaining the loss in photocatalytic activity over time. BJJ materials have been reported to show even more significant changes to their microstructure as evident from their PL spectra, indicating phase separation between the donor and acceptor components,^[29] highlighting the benefits of a single-component-type system.

2.3. Computational Predictions

We modeled **P40** as a tetramer with both the **Py** and phenyl pendant groups modeled explicitly (Figure S21, Supporting Information) using a previously developed approach based on Δ DFT (B3LYP)^[55–57] calculations on a single oligomer strand embedded in a dielectric continuum model to describe the effect of the reaction mixture the polymer particles are dispersed in.^[58,59] Using this approach, we predicted the IPs of **Py**, **P35**, and **P40** to be +0.86, +0.64, and +1.01 V, respectively, versus the standard hydrogen electrode (SHE) and the electron affinities (EAs) to be

−2.44, −1.92, −1.97 V, respectively, versus the SHE (Figure 2b; see Table S7, Supporting Information). While the EAs of **P35** and **P40** were determined to be comparable (−1.92 vs −1.97 V, respectively), the IPs, on the other hand were significantly different (+1.01 vs +0.64 V, respectively). We predict that after photoexcitation the hole localizes on the **Py** moiety while the electron delocalizes along the **FS** backbone. This localization of the hole on the **Py** moiety, rather than the **FS** backbone, would account for the comparatively shallow IP predicted for **P40** compared to **P35** and many other polymers possessing **FS** backbones.^[47,48] Moreover, the lowest energy conformer for **P40** was found to contort (Figure S21, Supporting Information), with the **Py** pendant groups forming intramolecular dimers, potentially causing the IP to move up in energy and may account as to why we predict the IP for **P40** to be shallower than that of isolated **Py**. It should be noted that we modeled **Py**, **P35**, and **P40** as isolated molecules/oligomers, rather than ensembles, which would result in a wider separation of the frontier energy levels.

The predicted optical gap of **P40**, the energy of the lowest energy vertical singlet-to-singlet excited state, obtained using time-dependent DFT (TD-DFT), as well as the predicted character of all the lowest excited states, was found to strongly depend on the density functional used. The issue here appears to be the well-known problem of TD-DFT to correctly describe the energies of charge-transfer excited-states,^[60] excited-states in which the hole and excited electron are spatially separated, relative to those of local excited states, where the hole and excited electron overlap. To circumvent this issue, we calculated the optical gap of the **P40** model instead using the wavefunction based spin-component scaled algebraic-diagrammatic-construction scheme of the polarization propagator of second order (SCS-ADC(2)) method.^[61–63] SCS-ADC(2) predicted that the optical gap corresponds to a local excitation where the hole and excited electron are both localized on the **Py**, with charge-transfer excitations, with the hole localized on the **Py** and the excited-electron delocalized over the **FS** backbone, and local excitations delocalized over the **FS** backbone lying slightly higher in energy (see Table S9 and Figures S22–S25, Supporting Information). After the initial excitation and internal conversion to the lowest excited state, the exciton separates with the excited electron transferring from **Py** to the **FS** backbone. Something that could possibly be facilitated by the charge-transfer excited state coming down in energy when the excited state relaxes.

In **P40**, the oscillator strength for the local **Py** to **Py** transitions were found to be two orders of magnitude lower than the **FS** to **FS** and the **Py** to **FS** transitions (see Table S9, Supporting Information). Therefore, we would expect these latter transitions to dominate the absorption spectrum of **P40**. This would explain why we observe similar absorption onsets for both **P35** and **P40** as the predicted excitation energies for these transitions are comparable in energy to the lowest excited state of **P35** (see Table S10, Supporting Information).

2.4. Transient Absorption Spectroscopy Experiments

Our models predicted a charge transfer process occurring after (or during) photoexcitation that could not be validated using steady-state optical measurements, such as UV–vis absorption and steady-state fluorescence spectroscopy, therefore, we

performed a deeper investigation into the photophysics of **P35** and **P40** using TAS. TAS measurements were recorded in the photocatalytic mixtures of 1:1:1 water/MeOH/TEA and a 2:1 water/MeOH mixture. It was not possible to record TAS data for **P40** in pure water as a sufficiently stable suspension could not be achieved for the duration of the experiment.

The TA spectra obtained for **P35** and **P40** in 1:1:1 water/MeOH/TEA have similar appearance to those of similar dibenzo[*b,d*]thiophene sulfone containing polymers reported previously,^[25,48,64] hence the spectral features are assigned in an analogous manner. Briefly, at the earliest times after excitation (0.5, 1 ps) the spectra (Figure 4a,b) are dominated by a broad photoinduced absorption (PIA) band with a peak at ≈800 and 820 nm, for **P35** and **P40**, respectively, assigned to the initially formed singlet local excited state, and negative signals at shorter wavelengths, which through comparison with the UV/vis spectra (Figure 2c) and the suspension-state PL spectra (Figure S18, Supporting Information), can be assigned to overlapping ground state bleach (GSB) and stimulated emission (SE). With increasing delay time, these features decay, and a PIA band at 610 and 625 nm, is observed for **P35** and **P40**, respectively, superimposed on the broad negative signal, which as in previous work, is assigned as the spectral signature of an electron polaron on the **FS** backbone.^[65] We show that for **P40** the intensity of this feature at the longest timescales probed (1 ns) is dependent on the volume of TEA in the solution, consistent with this assignment (Figures S28 and S29, Supporting Information).

We performed lifetime density analysis (LDA) of the TA data to provide further insight into the photodynamics of **P35** and **P40** (Figure 4c,d). LDA has been described in detail recently,^[66–70] and outlined within Section S5 (Supporting Information) of the accompanying ESI. The lifetime distributions are broad for all wavelengths (Figure 4c,d) with the breadth of kinetic processes observed resulting from LDA often correlated to dispersive kinetics,^[66,68,71] likely a result of structural disorder within the polymer particles. In the absence of TEA, a broad distribution of lifetimes, with a peak lifetime of ≈2.7 ps is observed in the 625 nm lifetime distribution (Figure S28e, Supporting Information). The lifetime averaged difference spectrum, (LADS) obtained for $\tau \approx 1 - 10$ ps shows only a weak negative going band at ≈625 nm, corresponding to the formation of the polaronic species, while the excitonic features decay. Owing to this, we conclude excitonic relaxation to the ground electronic state and excitonic dissociation to form partially-separated charges (i.e., polaron-pairs) on the polymer occur during these timescales; the weak negative going band at ≈625 nm observed in the LADS suggests that charge-separation is only a minor pathway for exciton relaxation. These species largely decay by 1 ns (further discussion is provided in Section S5.3 of the accompanying ESI); these observations are consistent with the poor photocatalytic activity of **P40** in the pure water and water/MeOH mixtures (Figure S40, Supporting Information). For **P35**, a similar, well-defined feature in the LADS is not observed, with only a minor deviation in the shape of the negative going signal between 575 and 700 nm observed for those obtained for during the 60 – 120 and 120 – 600 ps lifetimes, Figure S27e (Supporting Information). A weak, but clearly perceptible polaronic feature at ≈625 nm is observed for **P40** in the absence of TEA at the earliest timescale (0.5), Figure S28a (Supporting Information), appearing within

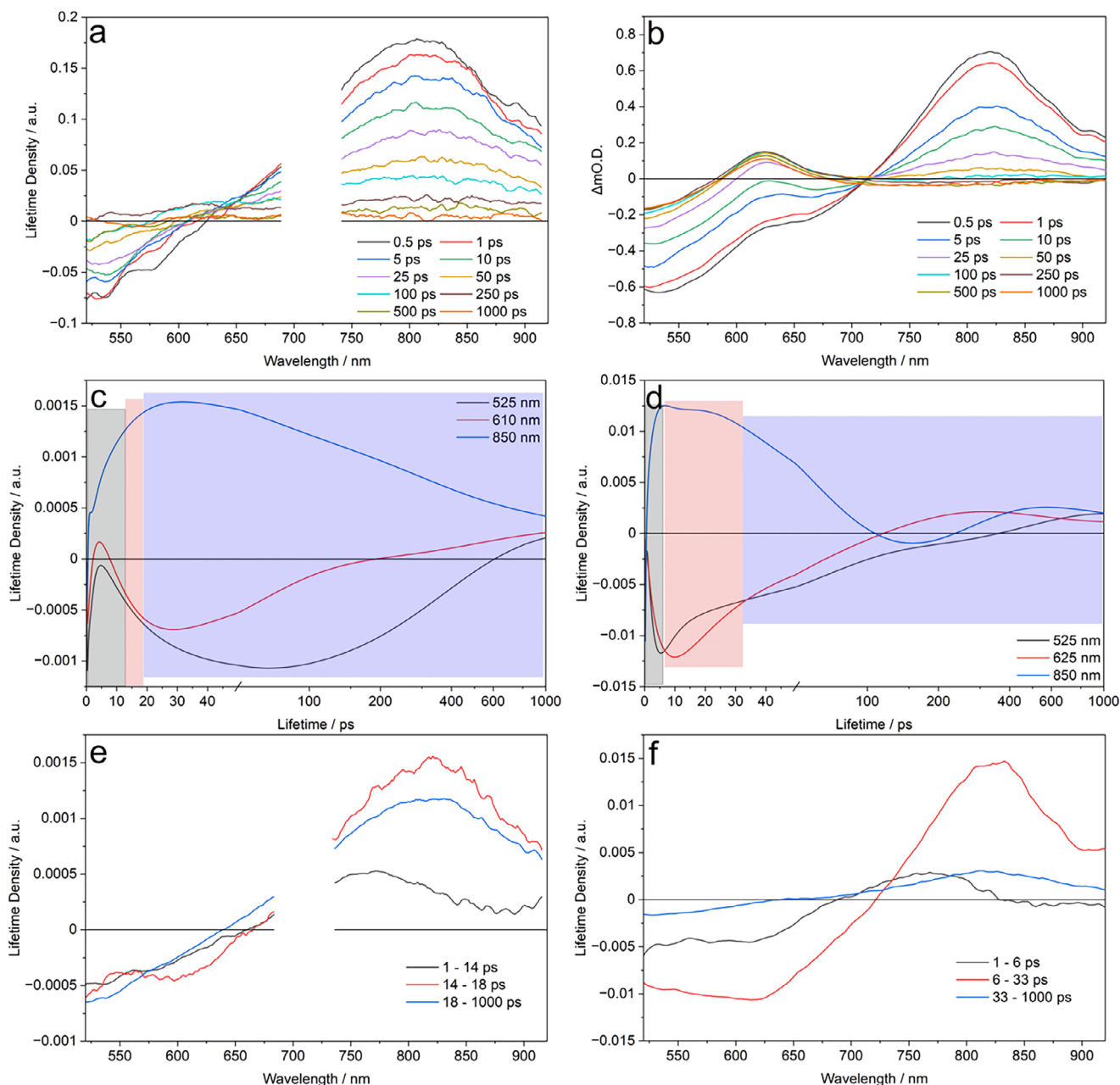


Figure 4. TA spectra at pump-probe time delays as indicated for in 1:1:1 water/MeOH/TEA for a) **P35** and b) **P40**. c) Lifetime distribution at 525, 610, and 850 nm obtained from lifetime density analysis of the TA spectra for **P35**. d) Lifetime distribution at 525, 630, and 850 nm obtained from lifetime density analysis of the TA spectra for **P40**. Lifetime averaged difference spectra obtained for the lifetime ranges as indicated, obtained from lifetime density analysis of e) **P35** and f) **P40** in 1:1:1 water/MeOH/TEA; the lifetime corresponding to these spectra are shown as colored panels in parts (c) and (d). For both **P35** and **P40** lifetimes where polaron formation occurs are highlighted within the area indicated in red in parts c and d. Data between 680 and 730 nm in parts a and e is contaminated by scattered pump light (2λ) and removed before analysis.

the instrument response function, IRF, (≈ 0.4 ps) which is absent for **P35**, Figure S27a (Supporting Information). Deconvolution of the IRF and coherent artifact(s) from the pure molecular response is challenging,^[67] hence owing to the time-resolution of the TA experiment we interpret the results of LDA for timescales > 1 ps. These differences in the photophysics of the two polymers indicate that charge-separation is more facile for **P40** than **P35**. This is consistent with the results of our calculations, which

suggest along with the backbone localized electronic transitions being optically allowed (monitored by the long wavelength transient PIA signature) for both polymers, charge-transfer states are also optically allowed for **P40**, explaining the spectral signature of the electron polaron at ≈ 625 nm, even at the earliest pump-probe delays, which is absent for **P35**.

For **P40**, in the 1:1:1 water/MeOH/TEA solution, as used in the photocatalysis experiments, the ≈ 625 nm polaronic band forms

within the IRF, as noted above, but as identified from the results of lifetime density analysis of the TA data, also on the 1 – 6 and 6 – 33 ps timescales (Figure 4f). We observed similar timescales for reductive quenching of the exciton of the homopolymer of dibenzo[*b,d*]thiophene sulfone, **P10**, recently.^[70] For **P35**, the TA spectra are remarkably similar in the presence and absence of TEA (Figure S26, Supporting Information). Lifetime density analysis of the TA data for **P35** indicates that excitonic quenching by TEA occurs between 14 and 18 ps (Figure 4c,e). However, the weak negative going signal observed for polaron formation indicates that this is only a minor pathway for exciton relaxation in **P35**, rationalizing the difference in activities of the two polymers in the 1:1:1 mixture.

Recently, we studied the kinetics of **P10** following 355 nm excitation in solutions containing ≈2% and 33% TEA by volume; in that case, we observed no difference in kinetics.^[70] We performed TA experiments of **P40** suspended in water/MeOH/TEA solutions containing a wide range of TEA volumes (0.003 – 33%), Figures S28 and S29 (Supporting Information); these results are described in detail in Section S5.3 of the accompanying ESI. Briefly, from LDA of these spectra, the peak lifetime for polaron formation is shown to be remarkably consistent ($\tau \approx 4 - 7$ ps) for the 0.05 – 13.3% TEA solutions, although we note the timescales for polaron formation are broad ($\tau \approx 1 - 10$ ps). Despite this, the intensity of the polaronic band is dependent on TEA volume (Figures S28–S31, Supporting Information). These observations are consistent with static quenching of the polymer exciton by TEA, with pre-association of **P40** and TEA being a prerequisite of this mechanism. The kinetics for the 33% TEA solution differs from this behavior, with little polaron formation occurring on the 1 – 10 ps, but is formed within the IRF and with a range of lifetimes between 10 and 20 ps. We explore this further in Sections 2.5 and 3.

2.5. Steady-State Photoluminescence in Suspension

We performed steady-state PL spectroscopy at 355 nm excitation in suspension (Figure S16, Supporting Information). In 2:1 water/MeOH, a band is observed with a peak at ≈475 nm, a weak tail extending into the visible, and a shoulder at ≈457 nm. However, when in the presence of TEA, the relative intensity of the long wavelength tail increases substantially; this long wavelength emission is absent from the spectra of **P35** (Figure S16, Supporting Information). The 457 and 475 nm features are consistent with vibrational progression observed for other copolymers containing the dibenzo[*b,d*]thiophene sulfone unit, whereas the unstructured longer wavelength emission is generally assigned to intrachain charge transfer states.^[64,72,73] However, we have recently shown that the profile of the emission spectra of **P10** appears to be independent of the solvent environment.^[70] As outlined above, **P10** displays similar timescales for reductive excitonic quenching and increased photocatalytic activity toward hydrogen evolution in the presence of TEA; hence, the assignment of the long wavelength emission to intrachain charge transfer states in **P40** is unlikely unless the presence of TEA changes the electronic and molecular structure of the **P40** aggregate via a mechanism not possible for **P10**.^[70] Long wavelength emissions in the range of 480 – 520 nm for Py containing solutions are often

assigned to the emission of excimers (Py-Py) and exciplexes (Py-TEA) in the presence of TEA,^[74,75] however, the precise nature of this emission is beyond the scope of this work.

We explored the influence of TEA concentration on the steady state fluorescence of **P35** and **P40** as suspensions in a 2:1 water/MeOH mixture (3 mL) in a cuvette (Figure 5). Unsurprisingly, we observe fluorescence quenching of both **P35** and **P40** upon the addition of TEA (Figure 5a,b), however, the extent of quenching is markedly different between **P35** and **P40** upon the initial addition of TEA (10 μL of TEA to 1 mL of the mixture). The PL intensity of **P35** at its emission maximum (I_{em}) decreased to ≈75% of its initial intensity, whereas **P40** showed a more dramatic decrease to ≈40% of its initial intensity. Subsequent additions of TEA had a diminished effect on the fluorescence quenching for both **P35** and **P40**. Such behavior is indicative of fractional accessibility of the quencher (TEA) to the fluorophores (polymer).^[76] This is unsurprising as it is unlikely that the TEA (or water/MeOH) can penetrate into the polymer particles to quench deeper situated fluorophores, a known issue of particulate photocatalysts.^[77] After normalizing the spectra of both **P35** and **P40** we also observed the relative growth in intensity of the long wavelength tail of the emission of **P40** upon the addition of TEA (Figure 5c,d). For clarity, we do not intend to imply that the intensity of emission has increased, rather the emission intensity at longer wavelengths appears to have increased relative to the emission maximum. This longer wavelength emission appears to be in line with our steady-state PL spectrum for **P40** suspended in a 1:1:1 water/TEA/MeOH mixture and, as discussed above, we believe this may be the consequence of a pre-association of TEA with the Py moieties on **P40**, as the rapid timescales for excitonic quenching by TEA observed for **P40** in our TA spectra is consistent with a significant degree of pre-association, as described in Section S1.4 and within Section S5.3 (Supporting Information) of the accompanying ESI.

To explore this further, we performed PL measurements at $I_{exc} = 355$ nm of **P40** as a suspension in water/MeOH/TEA solutions containing a range of TEA volumes similar to those studied using TA. The emission spectra obtained are shown in Figure S20 (Supporting Information). These experiments were obtained using a holder for front-face measurements of cuvettes containing highly absorbing liquids, removing the potential for inner-filter effects. The tilted sample configuration avoids direct reflection of excitation into emission channel; however, this makes precise placement between samples challenging, hence we do not compare the raw intensity of the emission. The results obtained for the 0 and 33% TEA solutions are remarkably similar to those described above (Figure S16, Supporting Information). Inclusion of just 0.03% TEA by volume, results in the long wavelength unstructured tail to be observed; interestingly, the 475 nm band also becomes clear. The 457 and 475 nm features are typically assigned to a vibrational progression in other copolymers containing the dibenzo[*b,d*]thiophene sulfone unit;^[64,72,73] the differing intensity of the two bands, which are largely unresolved in the 0% TEA solution (Figure S20, Supporting Information) on the addition of TEA is consistent with TEA changing the bond lengths, and hence (electronic) structure, of the polymer. As the volume of TEA is increased to 13% the intensity of the long wavelength band increases compared to the 475 nm band, with the intensity of the signal at ≈520 and 475 nm being notably similar in

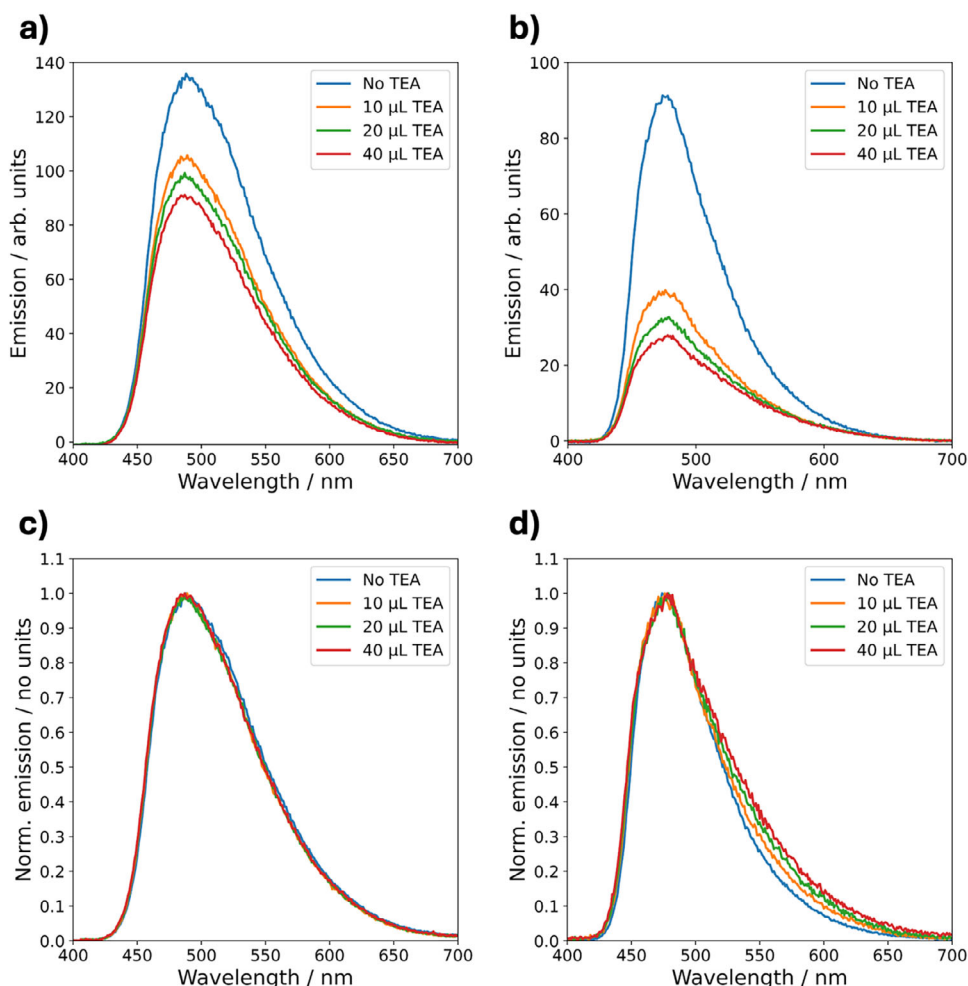


Figure 5. PL spectra of **P35** and **P40** suspended in 3 mL water/MeOH excited at 360 nm with additional TEA at specified quantities. The concentrations of the samples were 0.3 – 0.4 mg mL⁻¹ and the initial volume was 3 mL. The raw PL spectra of a) **P35** and b) **P40** with additional TEA added at specified quantities. (c) and (d) are the normalized spectra of (a) and (b), respectively. N.B. the profiles of **P35** overlay, whereas the relative intensity of the low energy tail increases upon addition of TEA for **P40**.

the 3.3 and 13% TEA solutions. This trend is reversed moving to the 33% TEA solution, where the signal at 475 nm is again more intense. It is clear that the observance of the 475 nm and unstructured long wavelength bands depend on the presence of TEA, but their differing relative intensities suggest they originate owing to different mechanisms, and/or several emissive transitions overlap. We note that there are two possible assignments for the long wavelength band emission: (i) intrachain charge transfer states or (ii) Py-TEA exciplex. It is interesting to note that the kinetics observed from the TA experiments in solutions containing 33% TEA also differ from those containing 0.05–13%.

3. Discussion

While the exceptionally high EQE observed for **P40** could be purely ascribed to efficient exciton dissociation facilitated by the predicted type-II energy level offset between the **FS** backbone and **Py** pendant groups, we also considered carefully the influence of **Py** within **P40**. We have separated the role of **Py** into three distinct factors: changes to the photophysics of the excited state, interac-

tions with the local solvent environment, and variations to the aggregate microstructure.

First, we consider the photophysics of the excited state of **P40**. In the ground state absorption and steady-state PL of the solid-state sample of **P40** (Figure 2c,d), it is clear that both **P35** and **P40** possess similar absorption profiles and that **P40** does not absorb further into the red region of the spectrum than **P35**, therefore ruling out improved light harvesting of longer wavelength photons as a potential cause for the high photocatalytic performance of **P40**. The difference in rate must therefore be a consequence of more efficient utilization of incident light, consistent with the larger EQE of **P40** than **P35**. For the TA spectra of **P40** in the absence of TEA we observe the signature of the electron polaron even at the earliest timescales (0.5 ps), which continues to grow over the next ≈ 10 ps. This does not occur for **P35**, suggesting polaron formation via exciton dissociation is more facile for **P40** than **P35**. Importantly, this is supported by our observations that suggests charge transfer occurs within **P40** after photoexcitation, where the excited electron and hole are separated to the **FS** backbone and **Py**, respectively; a process that cannot occur within **P35**.

Owing to the simple functionalization of the bridgehead carbon on fluorene, **FS**-type polymers have been studied extensively for side-chain engineering.^[48,64,78–80] Yet, the vast majority of these studies have targeted material processability and therefore focused on the use of flexible side chains, such as alkyl or oligo(ethylene glycol) groups, rather than large inflexible aromatic units, such as **Py**. We therefore must consider carefully the influence that **Py**, being a bulky hydrophobic pendant group, will have on the local solvent environment of **P40**. Given the hydrophobic nature of **Py**, **P40** tended to aggregate in pure water but dispersed well upon the addition of MeOH or TEA. This hydrophobicity may account, at least in part, for the absence of hydrogen when **P40** was tested for hydrogen evolution in the presence of ascorbic acid and the relatively low rate in the presence of triethanolamine (Figure S40, Supporting Information). Moreover, it may help to explain why TEA was an effective SED, as TEA is less polar it may interact more favorably with **P40** than **P35**. Previous studies using molecular dynamics have predicted that the local solvent environment surrounding a hydrophobic **FS**-type polymer with *n*-octyl side chains had a significantly larger proportion of TEA than MeOH or water, compared to a hydrophilic analogue with tri(ethylene glycol) side chains;^[48] therefore, we would expect a similar effect here for **P40**. We see evidence for this in our steady-state PL spectra in suspension as we observe the appearance of an emissive band at ≈ 520 nm when **P40** is suspended in a 1:1:1 water/TEA/MeOH mixture that is not present in the absence of TEA. A TEA concentration correlated emission in the wavelength region of 480–520 nm has previously been assigned to a **Py**-TEA exciplex emission that supports our suggestion.^[74] Moreover, our Δ DFT (B3LYP) and ADC(2) calculations suggest, as discussed above, that the holes will concentrate at the **Py** moieties, localizing the holes close to the SED, which has the potential to further accelerate reductive quenching. Alternately, unstructured longer wavelength emission is generally assigned to intrachain charge transfer states in polymers containing the dibenzo[*b,d*]thiophene sulfone unit. The increased intensity of this band compared to the narrower band at ≈ 470 nm with increasing TEA concentration may be explained by changing structure of the **P40** aggregate through intercalation of TEA (and likely MeOH and water) owing to the hydrophobicity of **P40** as hypothesized from MD simulations for other hydrophobic organic polymers. Such effects could induce profound changes in the intrachain interactions given the contorted lowest energy conformer calculated for **P40** (Figure S21, Supporting Information) enhancing intrachain charge transfer.^[64,72,73] Importantly, this red-shifted emission is absent for the suspension spectra of **P35** under identical conditions (Figure S16, Supporting Information). A pre-association of TEA to **P40** may partially account for the increased photocatalytic efficiency we observe as this would prime the material for reductive quenching. We note that the observance of this long wavelength tail (Figure S20, Supporting Information) and an increase in the 475 nm band intensity compared to the 457 nm shoulder in the PL spectrum coincides with the observance of changing kinetics observed in the TA experiments assigned to reductive quenching of the polymer exciton by TEA (Figures S27 and S28, Supporting Information). As noted above, the ps kinetics of **P40** in solutions containing 0.05–13% TEA differ from that in the 33% TEA solution. Consistent with this, the trends of the relative intensities of the broad unstruc-

tured long wavelength band and the 475 nm band in the PL, described in detail above, also change between solutions containing 13 and 33% TEA. It is clear that the volume of TEA in the solution has a complicated, multifaceted effect on the photophysics of **P40**. Finally, we consider the influence of **Py** on the microstructure of **P40**. **Py** is a large, inflexible polycyclic aromatic hydrocarbon; it will influence the packing of the polymer chains both due to steric effects and through π - π stacking. However, little information on the microstructure of **P40** can be gleaned due to its lack of long range order, therefore, we must make some assumptions based on what we understand for **Py** and **FS** polymer chains. As **Py** tends to form dimers in the condensed state, both molecular and as moieties, then we might also expect similar behavior in the **P40** aggregates.^[81] This is indeed what is observed in our low energy conformer used to predict the IP and EA of **P40**. Here, the **FS**-backbone contorts to allow for the **Py** pendants to form intramolecular dimers (see Figure S20, Supporting Information). The intra- and inter-chain interactions between **Py** moieties would then inhibit close stacking of polymer chains; potentially introducing voids within the particle aggregates that are responsible for the high SA_{BET} and microporosity we observe (Figures S10 and S11, Supporting Information). However, **P40** was found to be amorphous, making the confirmation of this difficult and regardless of this, recent work by McCulloch and co-workers suggests that the SA_{BET} determined by N_2 sorption isotherms correlate poorly with photocatalysts performance: rather it is the hydrophilic surface area determined by water sorption isotherms that is a more relevant metric for water splitting photocatalysts.^[82]

4. Solution-Processible Photocatalysts

We also present a set of soluble fluorene-based polymer analogues to demonstrate that the influence of **Py** pendant groups extends beyond their use in an **FS**-type polymer. These analogues were designed by substituting the dibenzo[*b,d*]thiophene sulfone repeat unit for an *n*-octyl (**P41**) or triethylene glycol (**P42**) functionalized fluorene unit, which makes these materials soluble in common organic solvents, such as chloroform and tetrahydrofuran. Additional polymers were also prepared for comparison, including **P43**, an alternating copolymer of di-*n*-octyl fluorene and spirobifluorene, and **P44**, an alternating copolymer of di-*n*-octyl fluorene and dimethyl fluorene. The chemical structures of **P41**–**P44** are outlined in Figure 6, and the synthetic details are presented in the Supporting Information. **P41** and **P43** have been previously reported elsewhere.^[83,84] Dispersions of powders of **P41**–**P44** were screened for sacrificial hydrogen evolution in the 1:1:1 water/TEA/MeOH mixture using a different photoreactor setup to that discussed above (see Supporting Information), therefore, direct comparison to the photocatalytic rates of **P35** and **P40** above should be avoided. **P41** and **P42** were found to generate hydrogen at rate of 212 and 1136 $\mu\text{mol h}^{-1} \text{g}^{-1}$, respectively. The higher photocatalytic hydrogen evolution rate of **P42** is unsurprising as it possesses tri(ethylene glycol) side chains that are known to be effective at improving photocatalytic performance for hydrogen evolution from water compared to their alkyl analogues.^[24,26,35,48,85] Importantly, **P41** and **P42** showed higher photocatalytic activity for hydrogen evolution than both **P43** (71 $\mu\text{mol h}^{-1} \text{g}^{-1}$) and **P44** (81 $\mu\text{mol h}^{-1} \text{g}^{-1}$). Moreover,

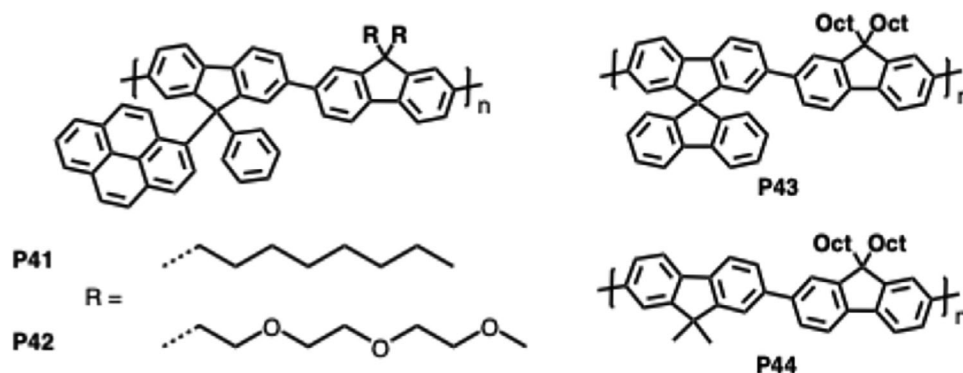


Figure 6. The chemical structures of P41 – P44.

the specific surface areas of **P41** and **P42** (determined by nitrogen sorption measurements) were higher than both **P43** and **P44** (Table S3, Supporting Information). Therefore, validating that the use of **Py** as a pendant can be an effective motif in the development of linear conjugated polymers photocatalysts for sacrificial hydrogen evolution.

5. Conclusion

Here, we present a single-component linear conjugated polymer photocatalyst, **P40**, in which a molecular donor, **Py**, was chemically tethered to a polymer acceptor, **FS**. **P40** demonstrated an impressive EQE for sacrificial hydrogen evolution from water of 38% at 420 nm; a value which, to our knowledge, is the highest reported value for any linear conjugated polymer to date. The results from our TA data suggest that there is better charge-separation in **P40** than in its analogue without the **Py** moieties, **P35**, in the absence of TEA. This result was consistent with our computational models that predict a charge transfer to occur after excitation within **P40** that resulted in the separation of photo-generated electrons and holes, with the photoelectrons localizing on the **FS** backbone and the holes localizing on the **Py** moieties. When in the presence of TEA, we observed evidence of efficient reductive exciton quenching of **P40** after photoexcitation in both our TA and steady-state PL results. We expect that this combination of charge transfer and efficient reductive quenching contributed to the enhanced photocatalytic efficiency of **P40**. Furthermore, we also found that **P40** had a specific surface area ≈ 3 times greater than the unfunctionalized analogue, **P35**; suggesting that the inclusion of **Py** in **P40** alters the microstructure of the polymer aggregate and facilitates porosity within the polymer particles. We believe that this also contributed to the enhanced photocatalytic activity of **P40**, compared to **P35**. This work demonstrates a unique polymer motif that influences the photophysics of the excited state and the polymer microstructure, resulting in enhanced photocatalytic efficiency for sacrificial hydrogen evolution.

Supporting Information

Supporting Information is available from the Wiley Online Library or from the author.

Acknowledgements

TA measurements were performed at the University of Liverpool Early Career Researcher Laser Laboratory supported by UKRI-EPSC grant EP/S017623/1 and the University of Liverpool, maintained and operated as a shared research facility by the Faculty of Science and Engineering. R.S.S. thanks the University of Strathclyde for financial support through The Strathclyde Chancellor's Fellowship Scheme and a Research Collaborations grant from the International Science Partnerships Fund (ID 1203758747). The grant was funded by the UK Department for Science Innovation and Technology in partnership with the British Council. A.I.C. thanks the Royal Society for a Research Professorship. E.M. thanks the EPSRC for funding through a Doctoral Training Partnership postgraduate studentship (EP/T517938/1). R.J.B. thanks the Hydro Nation Scholars Programme funded by the Scottish Government and managed by the Hydro Nation International Centre. This work used shared equipment located at the Materials Innovation Factory, which was created as part of the UK Research Partnership Innovation Fund (Research England) and co-funded by the Sir Henry Royce Institute. The authors thank Jing Yang, Yuan Li, and Owen Thwaites for their support of this work.

Conflict of Interest

The authors declare no conflict of interest.

Data Availability Statement

The data that support the findings of this study are available in the supplementary material of this article.

Keywords

conjugated polymers, hydrogen production, photocatalysis, photocatalyst

Received: May 23, 2025
Revised: November 26, 2025
Published online:

- [1] P. Erickson, M. Lazarus, G. Piggot, *Nat. Clim. Change* **2018**, *8*, 1037.
- [2] K. Engeland, M. Borga, J.-D. Creutin, B. François, M.-H. Ramos, J.-P. Vidal, *Renew. Sustain. Energy Rev.* **2017**, *79*, 600.
- [3] M. A. Habib, G. A. Q. Abdulrahman, A. B. S. Alqaity, N. A. A. Qasem, *Alex. Eng. J.* **2024**, *100*, 182.

- [4] I. Staffell, D. Scamman, A. Velazquez Abad, P. Balcombe, P. E. Dodds, P. Ekins, N. Shah, K. R. Ward, *Energy Environ. Sci.* **2019**, *12*, 463.
- [5] C. Smith, A. K. Hill, L. Torrente-Murciano, *Energy Environ. Sci.* **2020**, *13*, 331.
- [6] N. Rambhujun, M. S. Salman, T. Wang, C. Prathana, P. Sapkota, M. Costalin, Q. Lai, K.-F. Aguey-Zinsou, *MRS Energy Sustain.* **2020**, *7*, 33.
- [7] J. Manna, P. Jha, R. Sarkhel, C. Banerjee, A. K. Tripathi, M. R. Nouni, *Int. J. Hydrogen Energy* **2021**, *46*, 38212.
- [8] J. Gong, C. Li, M. R. Wasielewski, *Chem. Soc. Rev.* **2019**, *48*, 1862.
- [9] A. Fujishima, K. Honda, *Nature* **1972**, *238*, 37.
- [10] M. Sohail, S. Rauf, M. Irfan, A. Hayat, M. M. Alghamdi, A. A. El-Zahhar, D. Ghernaout, Y. Al-Hadeethi, W. Lv, *Nanoscale Adv.* **2024**, *6*, 1286.
- [11] Z. Wang, C. Li, K. Domen, *Chem. Soc. Rev.* **2019**, *48*, 2109.
- [12] L. Zhang, J. Zhang, H. Yu, J. Yu, *Adv. Mater.* **2022**, *34*, 2107668.
- [13] Y. Wang, A. Vogel, M. Sachs, R. S. Sprick, L. Wilbraham, S. J. A. Moniz, R. Godin, M. A. Zwijnenburg, J. R. Durrant, A. I. Cooper, *J. Tang, Nat. Energy* **2019**, *4*, 746.
- [14] Y.-N. Gong, X. Guan, H.-L. Jiang, *Coord. Chem. Rev.* **2023**, *475*, 214889.
- [15] S. Luo, Z. Zeng, G. Zeng, Z. Liu, R. Xiao, P. Xu, H. Wang, D. Huang, Y. Liu, B. Shao, Q. Liang, D. Wang, Q. He, L. Qin, Y. Fu, *J. Mater. Chem. A* **2020**, *8*, 6434.
- [16] J. M. Lee, A. I. Cooper, *Chem. Rev.* **2020**, *120*, 2171.
- [17] C. M. Aitchison, C. M. Kane, D. P. McMahon, P. R. Spackman, A. Pulido, X. Wang, L. Wilbraham, L. Chen, R. Clowes, M. A. Zwijnenburg, R. S. Sprick, M. A. Little, G. M. Day, A. I. Cooper, *J. Mater. Chem. A* **2020**, *8*, 7158.
- [18] H. Yang, C. Li, T. Liu, T. Fellowes, S. Y. Chong, L. Catalano, M. Bahri, W. Zhang, Y. Xu, L. Liu, W. Zhao, A. M. Gardner, R. Clowes, N. D. Browning, X. Li, A. J. Cowan, A. I. Cooper, *Nat. Nanotechnol.* **2023**, *18*, 307.
- [19] Q. Zhou, Y. Guo, Y. Zhu, *Nat. Catal.* **2023**, *6*, 574.
- [20] W. Zhang, M. Yu, T. Liu, M. Cong, X. Liu, H. Yang, Y. Bai, Q. Zhu, S. Zhang, H. Gu, X. Wu, Z. Zhang, Y. Wu, H. Tian, X. Li, W.-H. Zhu, A. I. Cooper, *Nat. Synth.* **2024**, *3*, 595.
- [21] C.-L. Chang, W.-C. Lin, L.-Y. Ting, C.-H. Shih, S.-Y. Chen, T.-F. Huang, H. Tatenjo, J. Jayakumar, W.-Y. Jao, C.-W. Tai, C.-Y. Chu, C.-W. Chen, C.-H. Yu, Y.-J. Lu, C.-C. Hu, A. M. Elewa, T. Mochizuki, H.-H. Chou, *Nat. Commun.* **2022**, *13*, 5460.
- [22] W.-C. Lin, C.-L. Chang, C.-H. Shih, W.-C. Lin, Z. Yu Lai, J.-W. Chang, L.-Y. Ting, T.-F. Huang, Y.-E. Sun, H.-Y. Huang, Y.-T. Lin, J.-J. Liu, Y.-H. Wu, Y.-T. Tseng, Y.-R. Zhuang, B.-H. Li, A.-C. Su, C.-H. Yu, C.-W. Chen, K.-H. Lin, U.-S. Jeng, H.-H. Chou, *Small* **2023**, *19*, 0230615.
- [23] W.-H. Wang, L.-Y. Ting, J. Jayakumar, C.-L. Chang, W.-C. Lin, C.-C. Chung, M. H. Elsayed, C.-Y. Lu, A. M. Elewa, H.-H. Chou, *Sustain. Energy Fuels* **2020**, *4*, 5264.
- [24] R. J. Lyons, Y. Yang, E. McQueen, L. Luo, A. I. Cooper, M. A. Zwijnenburg, R. S. Sprick, *Adv. Energy Mater.* **2024**, *14*, 2303680.
- [25] M. Sachs, R. S. Sprick, D. Pearce, S. A. J. Hillman, A. Monti, A. A. Y. Guilbert, N. J. Brownbill, S. Dimitrov, X. Shi, F. Blanc, M. A. Zwijnenburg, J. Nelson, J. R. Durrant, A. I. Cooper, *Nat. Commun.* **2018**, *9*, 4968.
- [26] M. Yu, W. Zhang, Z. Guo, Y. Wu, W. Zhu, *Angew. Chem., Int. Ed.* **2021**, *60*, 15590.
- [27] J. Kosco, M. Bidwell, H. Cha, T. Martin, C. T. Howells, M. Sachs, D. H. Anjum, S. Gonzalez Lopez, L. Zou, A. Wadsworth, W. Zhang, L. Zhang, J. Tellam, R. Sougrat, F. Laquai, D. M. DeLongchamp, J. R. Durrant, I. McCulloch, *Nat. Mater.* **2020**, *19*, 559.
- [28] J. Kosco, S. Gonzalez-Carrero, C. T. Howells, T. Fei, Y. Dong, R. Sougrat, G. T. Harrison, Y. Firdaus, R. Sheelamantula, B. Purushothaman, F. Moruzzi, W. Xu, L. Zhao, A. Basu, S. De Wolf, T. D. Anthopoulos, J. R. Durrant, I. McCulloch, *Nat. Energy* **2022**, *7*, 340.
- [29] J. R. Mistry, E. McQueen, F. Nudelman, R. S. Sprick, I. A. Wright, *J. Mater. Chem A Mater.* **2024**, *12*, 23411.
- [30] W.-C. Lin, Y.-E. Sun, Y.-R. Zhuang, T.-F. Huang, K.-J. Lin, M. M. Elsenety, J.-C. Yen, H.-K. Hsu, B.-H. Chen, C.-Y. Chang, J.-W. Chang, H.-N. Huang, B.-H. Li, S. Jungsuttiwong, T. Haldar, S.-H. Wang, W.-C. Lin, T.-L. Wu, C.-W. Chen, C.-H. Yu, A.-C. Su, K.-H. Lin, U.-S. Jeng, S.-D. Yang, H.-H. Chou, *J. Am. Chem. Soc.* **2025**, *147*, 2537.
- [31] M. Yu, W. Zhang, X. Liu, G. Zhao, J. Du, Y. Wu, W.-H. Zhu, *Green Energy Environ.* **2025**, *10*, 390.
- [32] J. Kosco, S. Gonzalez-Carrero, C. T. Howells, W. Zhang, M. Moser, R. Sheelamantula, L. Zhao, B. Willner, T. C. Hidalgo, H. Faber, B. Purushothaman, M. Sachs, H. Cha, R. Sougrat, T. D. Anthopoulos, S. Inal, J. R. Durrant, I. McCulloch, *Adv. Mater.* **2021**, *34*, 2105007.
- [33] J. Choi, W. Jung, S. Gonzalez-Carrero, J. R. Durrant, H. Cha, T. Park, *Energy Environ. Sci.* **2024**, *17*, 7999.
- [34] S. Kang, T. W. Yoon, G.-Y. Kim, B. Kang, *ACS Appl. Nano Mater.* **2022**, *5*, 17436.
- [35] S. An, Z. Wu, H. Jeong, J. Lee, S. Y. Jeong, W. Lee, S. Kim, J. W. Han, J. Lim, H. Cha, H. Y. Woo, D. S. Chung, *Small* **2023**, *19*, 2204905.
- [36] A. Dolan, J. M. de la Perrelle, T. D. Small, E. R. Milsom, G. F. Metha, X. Pan, M. R. Andersson, D. M. Huang, T. W. Kee, *ACS Appl. Nano Mater.* **2022**, *5*, 12154.
- [37] Y. Yang, D. Li, P. Wang, X. Zhang, H. Zhang, B. Du, C. Guo, T. Wang, D. Liu, *Polymer* **2022**, *244*, 124667.
- [38] M. H. Elsayed, M. Abdellah, A. Z. Alhakemy, I. M. A. Mekhemer, A. E. A. Aboubakar, B.-H. Chen, A. Sabbah, K.-H. Lin, W.-S. Chiu, S.-J. Lin, C.-Y. Chu, C.-H. Lu, S.-D. Yang, M. G. Mohamed, S.-W. Kuo, C.-H. Hung, L.-C. Chen, K.-H. Chen, H.-H. Chou, *Nat. Commun.* **2024**, *15*, 707.
- [39] M. V. Pavliuk, M. Böhm, J. Wilhelmsen, S. Hardt, H. Land, H. Tian, *Chem. Sci.* **2024**, *15*, 16789.
- [40] Y. Yang, M. A. Zwijnenburg, A. M. Gardner, S. Adamczyk, J. Yang, Y. Sun, Q. Jiang, A. J. Cowan, R. S. Sprick, L.-N. Liu, A. I. Cooper, *ACS Nano* **2024**, *18*, 13484.
- [41] A. Liu, L. Gedda, M. Axelsson, M. Pavliuk, K. Edwards, L. Hammarström, H. Tian, *J. Am. Chem. Soc.* **2021**, *143*, 2875.
- [42] C. M. Aitchison, S. Gonzalez-Carrero, S. Yao, M. Benkert, Z. Ding, N. P. Young, B. Willner, F. Moruzzi, Y. Lin, J. Tian, P. D. Nellist, J. R. Durrant, I. McCulloch, *Adv. Mater.* **2023**, *36*, 2300037.
- [43] Y. He, N. Li, T. Heumüller, J. Wortmann, B. Hanisch, A. Aubele, S. Lucas, G. Feng, X. Jiang, W. Li, P. Bäuerle, C. J. Brabec, *Joule* **2022**, *6*, 1160.
- [44] J. Roncali, I. Grosu, *Adv. Sci.* **2019**, *6*, 1801026.
- [45] R. Goy, L. Bertini, T. Rudolph, S. Lin, M. Schulz, G. Zampella, B. Dietzek, F. H. Schacher, L. De Gioia, K. Sakai, W. Weigand, *Chem.-Eur. J.* **2017**, *23*, 334.
- [46] Y. Wang, C.-E. Wang, W.-R. Wang, Q. Li, L.-N. Liu, Z.-W. Xu, T.-Z. Gao, Y.-F. Wang, W.-S. Li, *Polymer* **2024**, *308*, 127334.
- [47] Y. Bai, L. Wilbraham, H. Gao, R. Clowes, H. Yang, M. A. Zwijnenburg, A. I. Cooper, R. S. Sprick, *J. Mater. Chem. A* **2021**, *9*, 19958.
- [48] D. J. Woods, S. A. J. Hillman, D. Pearce, L. Wilbraham, L. Q. Flagg, W. Duffy, I. McCulloch, J. R. Durrant, A. A. Y. Guilbert, M. A. Zwijnenburg, R. S. Sprick, J. Nelson, A. I. Cooper, *Energy Environ. Sci.* **2020**, *13*, 1843.
- [49] J. Kosco, I. McCulloch, *ACS Energy Lett.* **2018**, *3*, 2846.
- [50] J. Kosco, M. Sachs, R. Godin, M. Kirkus, L. Francas, M. Bidwell, M. Qureshi, D. Anjum, J. R. Durrant, I. McCulloch, *Adv. Energy Mater.* **2018**, *8*, 1802181.
- [51] M. Sachs, H. Cha, J. Kosco, C. M. Aitchison, L. Francàs, S. Corby, C.-L. Chiang, A. A. Wilson, R. Godin, A. Fahey-Williams, A. I. Cooper, R. S. Sprick, I. McCulloch, J. R. Durrant, *J. Am. Chem. Soc.* **2020**, *142*, 14574.
- [52] J. Yang, D. Wang, H. Han, C. Li, *Acc. Chem. Res.* **2013**, *46*, 1900.
- [53] C. Han, S. Xiang, S. Jin, L.-W. Luo, C. Zhang, C. Yan, J.-X. Jiang, *J. Mater. Chem. A* **2022**, *10*, 5255.

- [54] C. Li, J. Liu, H. Li, K. Wu, J. Wang, Q. Yang, *Nat. Commun.* **2022**, *13*, 2357.
- [55] A. D. Becke, *J. Chem. Phys.* **1993**, *98*, 5648.
- [56] C. Lee, W. Yang, R. G. Parr, *Phys. Rev. B* **1988**, *37*, 785.
- [57] S. H. Vosko, L. Wilk, M. Nusair, *Can. J. Phys.* **1980**, *58*, 1200.
- [58] P. Guiglion, C. Butchosa, M. A. Zwijnenburg, *J. Mater. Chem. A* **2014**, *2*, 11996.
- [59] P. Guiglion, A. Monti, M. A. Zwijnenburg, *J. Phys. Chem. C* **2017**, *121*, 1498.
- [60] M. J. G. Peach, P. Benfield, T. Helgaker, D. J. Tozer, *J. Chem. Phys.* **2008**, *128*, 044118.
- [61] A. B. Trofimov, J. Schirmer, *J. Phys. B: At., Mol. Opt. Phys.* **1995**, *28*, 2299.
- [62] S. Grimme, L. Goerigk, R. F. Fink, *WIREs Comput. Mol. Sci.* **2012**, *2*, 886.
- [63] A. Tajti, L. Tulipán, P. G. Szalay, *J. Chem. Theory Comput.* **2020**, *16*, 468.
- [64] S. A. J. Hillman, R. S. Sprick, D. Pearce, D. J. Woods, W.-Y. Sit, X. Shi, A. I. Cooper, J. R. Durrant, J. Nelson, *J. Am. Chem. Soc.* **2022**, *144*, 19382.
- [65] V. L. Piercy, K. H. Saeed, A. W. Prentice, G. Neri, C. Li, A. M. Gardner, Y. Bai, R. S. Sprick, I. V. Sazanovich, A. I. Cooper, M. J. Rosseinsky, M. A. Zwijnenburg, A. J. Cowan, *J. Phys. Chem. Lett.* **2021**, *12*, 10899.
- [66] O. Thwaites, B. M. Christianson, A. J. Cowan, F. Jäckel, L.-N. Liu, A. M. Gardner, *J. Phys. Chem. B* **2023**, *127*, 7283.
- [67] C. Slavov, H. Hartmann, J. Wachtveitl, *Anal. Chem.* **2015**, *87*, 2328.
- [68] M. Forster, D. W. F. Cheung, A. M. Gardner, A. J. Cowan, *J. Chem. Phys.* **2020**, *153*, 150901.
- [69] C. Li, A. J. Cowan, A. M. Gardner, *Chem. Phys. Rev.* **2022**, *3*, 031304.
- [70] R. J. Lyons, E. McQueen, R. J. Bourhill, O. Thwaites, A. I. Cooper, R. S. Sprick, A. J. Cowan, A. M. Gardner, *J. Chem. Phys.* **2025**, *163*, 044706.
- [71] C. Slavov, T. Fischer, A. Barnoy, H. Shin, A. G. Rao, C. Wiebeler, X. Zeng, Y. Sun, Q. Xu, A. Gutt, K.-H. Zhao, W. Gärtner, X. Yang, I. Schapiro, J. Wachtveitl, *Proc. Natl. Acad. Sci., U. S. A.* **2020**, *117*, 16356.
- [72] F. B. Dias, S. King, A. P. Monkman, I. I. Perepichka, M. A. Kryuchkov, I. F. Perepichka, M. R. Bryce, *J. Phys. Chem. B* **2008**, *112*, 6557.
- [73] F. B. Dias, S. Pollock, G. Hedley, L.-O. Pålsson, A. Monkman, I. I. Perepichka, I. F. Perepichka, M. Tavasli, M. R. Bryce, *J. Phys. Chem. B* **2006**, *110*, 19329.
- [74] M. Kumar, S. Pandey, *J. Phys. Chem. B* **2024**, *128*, 8040.
- [75] E. Folgado, M. Guerre, N. Mimouni, V. Collière, C. Bijani, K. Moineau-Chane Ching, A.-M. Caminade, V. Ladmiraal, B. Améduri, A. Ouali, *ChemPlusChem* **2019**, *84*, 78.
- [76] S. E. Webber, *Photochem. Photobiol.* **1997**, *65*, 33.
- [77] R. J. Lyons, R. S. Sprick, *Mater. Horiz.* **2024**, *11*, 3764.
- [78] C. Dai, S. Xu, W. Liu, X. Gong, M. Panahandeh-Fard, Z. Liu, D. Zhang, C. Xue, K. P. Loh, B. Liu, *Small* **2018**, *14*, 1801839.
- [79] R. Li, C. Zhang, C.-X. Cui, Y. Hou, H. Niu, C.-H. Tan, X. Yang, F. Huang, J.-X. Jiang, Y. Zhang, *Polymer* **2022**, *240*, 124509;.
- [80] R. Li, X. Zhang, C. Zhang, J. Lu, J.-C. Wang, C.-X. Cui, X. Yang, F. Huang, J.-X. Jiang, Y. Zhang, *Int. J. Hydrogen Energy* **2022**, *47*, 29771.
- [81] X. Feng, X. Wang, C. Redshaw, B. Z. Tang, *Chem. Soc. Rev.* **2023**, *52*, 6715.
- [82] B. J. Willner, C. M. Aitchison, F. Podjaski, W. Lu, J. Tian, J. R. Durrant, I. McCulloch, *J. Am. Chem. Soc.* **2024**, *146*, 30813.
- [83] D. M. E. Freeman, A. J. Musser, J. M. Frost, H. L. Stern, A. K. Forster, K. J. Fallon, A. G. Rapis, F. Cacialli, I. McCulloch, T. M. Clarke, R. H. Friend, H. Bronstein, *J. Am. Chem. Soc.* **2017**, *139*, 11073.
- [84] C. Tang, H. Xu, F. Liu, X.-D. Liu, W.-Y. Lai, X.-L. Wang, W. Huang, *Synth. Met.* **2013**, *174*, 33.
- [85] Z. Hu, Z. Wang, X. Zhang, H. Tang, X. Liu, F. Huang, Y. Cao, *iScience* **2019**, *13*, 33.